Operando Monitoring of Homolytic Cleavage of H2 into Surface Hydrides on Defective Cerium Dioxide Nanoparticles

Rémi André, Jean-Jacques Gallet, Fabrice Bournel, Sophie Carenco

Operando Monitoring of Homolytic Cleavage of H_2 into Surface Hydrides on Defective Cerium Dioxide Nanoparticles

Rémi F. André,[1] Jean-Jacques Gallet,[2,3] Fabrice Bournel,[2,3] Sophie Carenco,[1,]*

[1] Sorbonne Université, CNRS, Laboratoire de Chimie de la Matière Condensée de Paris (LCMCP), 4 place Jussieu, 75005 Paris, France

[2] Sorbonne Université, CNRS, Laboratoire de Chimie Physique Matière et Rayonnement (LCPMR), 4 place Jussieu, 75005 Paris, France

[3] Synchrotron SOLEIL, L'Orme des Merisiers, 91910 St Aubin, France

*Corresponding author. E-mail: sophie.carenco@sorbonne-universite.fr

Abstract:

The use of ceria as catalyst in hydrogenation reactions is a recent trend, as they were uncovered to be active on a number of substrates, including alkynes, alkenes, and enones. While some studies focused on the use of well-defined shapes, others emphasized the interest of defective structures. Overall, the meeting point of these studies is the need to characterize the surface reactivity *vs.* H_2, by considering a number of interesting textures (films, nanopowders with various grain size or porosity), using monitoring techniques that preserve the original features of the materials. A key question is in particular to assess the possibility to form surface hydride through homolytic H_2 splitting at cerium sites rather than at the oxygen one, a route recently highlighted as plausible.

To address this question on small crystallites of CeO_2, we designed a low-temperature synthetic route for nanorods with an average grain size of 10 nm. Then, we employed near-

ambient-pressure X-ray photoelectron spectroscopy as an *operando* tool to monitor the cerium surface oxidation state during the initial annealing of the nanopowders, followed by exposure to a moderate pressure of H_2 (0.52 mbar). We demonstrate that H_2 homolytic splitting at cerium sites is the main activation process on this surface at 100 °C, leading to the oxidation of *ca.* 30% of the surface cerium atoms from Ce^{3+} to Ce^{4+}. The surface hydride species were however not stable at 250 °C, H_2 was released, and cerium reduced back to Ce^{3+}. A similar mechanism was observed on a defective ceria material obtained by calcination of $CeO(OH)_2$, with comparable intensities. Overall, we report here CeO_2 nanorods, exposing predominantly {100} and {110} facets, as showing an interesting surface reactivity for potential application in hydrogenation reactions, and we expose a straight *operando* methodology to delineate suitable temperatures to be used.

Keywords: cerium dioxide, homolytic cleavage, NAP-XPS, surface hydride

1. Introduction

Cerium dioxide (CeO_2) exhibits interesting catalytic performances attributable to the dual oxidation states of cerium, facilitating the presence of a substantial concentration of oxygen vacancies and a complex redox chemistry.[1–3] Traditionally, CeO_2 has primarily served as a catalytic support; however, it has also emerged as a stand-alone catalyst for H_2 activation both for liquid-phase and gas-phase semi-hydrogenation of alkynes, which opened a new field of research for this rare earth oxide.[4–6] Pérez-Ramírez *et al.*, in particular, investigated the conversion of alkynes (propyne, ethyne) to olefins with excellent selectivites on commercial CeO_2 nanopowder.[7] They further demonstrated the importance of the particle morphology as the {111} facets exposed by CeO_2 polyhedra appeared more favorable for acetylene hydrogenation than the {100} ones, predominantly exposed by nanocubes.[8] This observation aligns with the findings of Lu *et al.*, who reported an increasing catalytic activity, with the following trend: CeO_2 cubes < CeO_2 polyhedra < CeO_2 rods ({100} and {220} facets), for crotonaldehyde hydrogenation.[9] The dependance of the catalytic activity of the ceria as a function of the oxygen vacancies concentration nonetheless differs according to the reaction. Indeed, Pérez-Ramírez *et al.* reported that a too strong reduction of the material (associated with defects creation) was detrimental to H_2 activation, whereas Lu *et al.* stressed the importance of the oxygen vacancies stabilized on {110} facets, in order to create solid frustrated Lewis pair (FLP) sites to promote the heterolytic cleavage of hydrogen at low temperatures.

Different mechanisms may be considered for hydrogen activation: the homolytic dissociation at two oxygen sites to form two hydroxyl groups (OH), associated with the reduction of Ce^{4+} centers in Ce^{3+} (Eq. (1)), the heterolytic dissociation to form both hydroxyl and a hydride species (Ce–H) (Eq. (2)), the homolytic dissociation to form two hydrides (Eq. (3)), and the oxygen vacancy formation upon release of a water molecule (Eq. (4)).[10] Note

that only the homolytic dissociation to Ce–H requires Ce^{3+} centers beforehand and leads to formal oxidation to Ce^{4+}. The hydride species are then stabilized in an oxygen vacancy V_O.

$$H_{2\,(g)} + 2\,Ce^{4+} + 2\,O^{2-} \rightarrow 2\,Ce^{3+} + 2\,OH^{-} \quad (1)$$

$$H_{2\,(g)} + Ce^{4+} + O^{2-} \rightarrow (Ce^{4+} - H^{-}) + OH^{-} \quad (2)$$

$$H_{2\,(g)} + 2\,Ce^{3+} \rightarrow 2\,(Ce^{4+} - H^{-}) \quad (3)$$

$$H_{2\,(g)} + 2\,Ce^{4+} + O^{2-} \rightarrow 2\,Ce^{3+} + H_2O + V_O \quad (4)$$

The first direct spectroscopic evidence of the existence of both surface and bulk Ce–H species was provided by Ramirez-Cuesta *et al.* using inelastic neutron scattering spectroscopy.[11] Since then, this mechanism of hydride formation on deficient ceria attracted growing interest for the catalytic hydrogenation of acetylene and propyne,[12,13] and led to density functional theory (DFT) modeling for different Ce environments,[14] Near-Ambient Pressure-X–ray Photoelectron Spectroscopy (NAP-XPS) analysis of ceria thin films (Ce 4d region and valence band),[15] and to the study of the influence of the presence of copper clusters deposited on CeO_2 for hydride stabilization.[16] Recently, Freund *et al.* provided experimental proof of the homolytic dissociation of H_2 in stable surface hydrides on ceria (Eq. (3)) in the presence of oxygen vacancies, adding a possible elementary step to the rich reactivity of cerium oxide surfaces.[10,17,18] Such a dissociation was mainly inferred from the increase of the surface Ce^{4+} concentration upon addition of H_2 in the mbar regime. The mechanisms were mainly discussed through XPS experiments revealing the cerium oxidation state, and infrared spectroscopy to probe surface hydroxyl species.

These mechanistic investigations were conducted on CeO_2 thin films or commercial powders composed of CeO_2 irregular polyhedra and spheres with fairly large crystallites. However, it is known that the reactivity of cerium oxide is strongly correlated to the texture, crystallinity, and morphological features of the materials. It is unclear if the conclusions reached on these

studies would still stand on smaller CeO_2 nanoparticles and on CeO_2 nanorods, previously reported as one of the best phase for crotonaldehyde hydrogenation, considering that defects and porosity may also be used to generate active hydrogenation catalysts.[6] Moreover, previous investigations mostly relied on *ex situ* XPS measurements. NAP–XPS, nowadays readily available, offers the advantage of *operando* observations, which can be performed under softer conditions, thus limiting possible modification of the texture and crystallinity as a consequence of intermediate treatment. Indeed, small crystallites are known to be strongly sensitive to operating conditions.[19] Thus, it is timely and enlightening for the community interested in CeO_2 hydrogenation capability to provide a clearer understanding of H_2 interaction with another texture of cerium oxide, if possible under *operando* conditions, under various temperatures and H_2 pressures.

In this study, we propose to assess the robustness of the described mechanisms by studying *via* NAP-XPS the interaction of H_2 with two CeO_2 samples, synthesized in-house following a hydrothermal path: one representative of a classical pathway and yielding CeO_2 nanorods and cubes, the other *via* a cerium oxyhydroxide phase and yielding highly defective materials, following a recent work from Qu *et al.*[6] We focused on the analysis of the Ce 3d and O 1s regions at an H_2 pressure of 0.52 mbar after calcination under ultra-high vacuum (UHV). Our experiments first confirmed that hydrogen activation resulted in the formation of surface hydride. Furthermore, we found that the extent of this phenomenon was dramatically increased on CeO_2 nanorods *vs.* the reported observations made on commercial powders.

2. Results and discussion

2.1. Cerium oxides syntheses and calcination

Cerium dioxide nanoparticles (CeO_2 NPs) were first directly synthesized by hydrothermal treatment of $Ce(NO_3)_3 \cdot 6H_2O$ with a 6 M NaOH solution at 100 °C (see experimental section)

(Figure 1**A**).[20] The material is isostructural with CeO_2 [PDF card N°00-034-0394], with a crystallite size of *ca.* 10 nm according to the Scherrer formula applied to the peaks at 29°, 33°, 47° and 69° (Figure 1**B**). However, the exact determination of the Ce:O ratio is not possible by X–Ray Diffraction (XRD) as CeO_2 may accommodate a large number of oxygen vacancies to form CeO_{2-x} ($0 < x < 0.5$).[21] The nitrogen sorption isotherm recorded at 77 K is of type II, *i.e.* non-porous or macroporous, which agrees with pores only generated upon aggregation of the NPs. The surface area determined following Brunauer-Emmett-Teller analysis applied on the low-pressure region is of 91 $m^2 \cdot g^{-1}$ (**Figure S1**). The analysis of the material by laboratory XPS confirmed the absence of any metal contaminants at the surface, as none was detected in the survey spectrum (**Figure S2,3**). Transmission Electron Microscopy (TEM) reveals the particles consist in polycrystalline nanorods (100–200 nm long × 10 nm wide) and to a smaller extent in nanocubes (10–20 nm in diameter) (Figure 1**C**). Because the crystallites are in average much smaller than the particles, these morphologies imply the presence of numerous grain boundaries, which are as many sites facilitating the stabilization of surface defects. High-Resolution TEM (HRTEM) analysis confirmed the diversity of exposed facets, with for instance the detection of (111) and (200) electron diffraction fringes parallel to the surface (Figure 1**E-F).** The corresponding Fourier Transform reveals maxima in all the possible diffraction rings (Figure 1**G).** Interestingly, Wöll *et al.* proved on similar CeO_2 samples (nanorods decorated with cubes), using CO as a probe molecule in Fourier Transform Infrared (FTIR) spectroscopy experiments, that the preferentially exposed facets were (110) and (111), and with only a minor contribution of (100) ones.[22] Upon annealing at 527 °C, the ceria nanorods reconstructed to expose (111) "nanofacets" of only several atoms width.

The CeO_2 NPs were aimed at being studied after calcination at 500 °C. Their structural stability was therefore first assessed *ex situ* by thermal treatment under vacuum at different temperatures (100 °C, 200 °C and 500 °C) for 2 h. A treatment at only 100 °C did not affect

the color of the powder. In contrast with this, the powder first turned grey and then violet after a few minutes at 200 °C or 500 °C (Figure 1**B,** inset), a color characteristic of the presence of reduced cerium Ce^{3+}.[23] The color persisted over weeks if the compound was stored in argon but the powder instantaneously turned back to yellow when exposed to air. XRD was performed after a stronger treatment of the powder, at 500 °C for 2 h under vacuum. The diffractogram showed that the phase was preserved but the crystallite size slightly increased to 13 nm. According to TEM, the morphology was also preserved with no substantial modification (Figure 1**D**), attesting to the structural integrity of the CeO_2 nanoparticles and consistent with their ability to maintain small crystallite domains despite the elevated temperature. Unless otherwise stated, CeO_2 NPs in the following designates this sample CeO_2 nanorods + cubes.

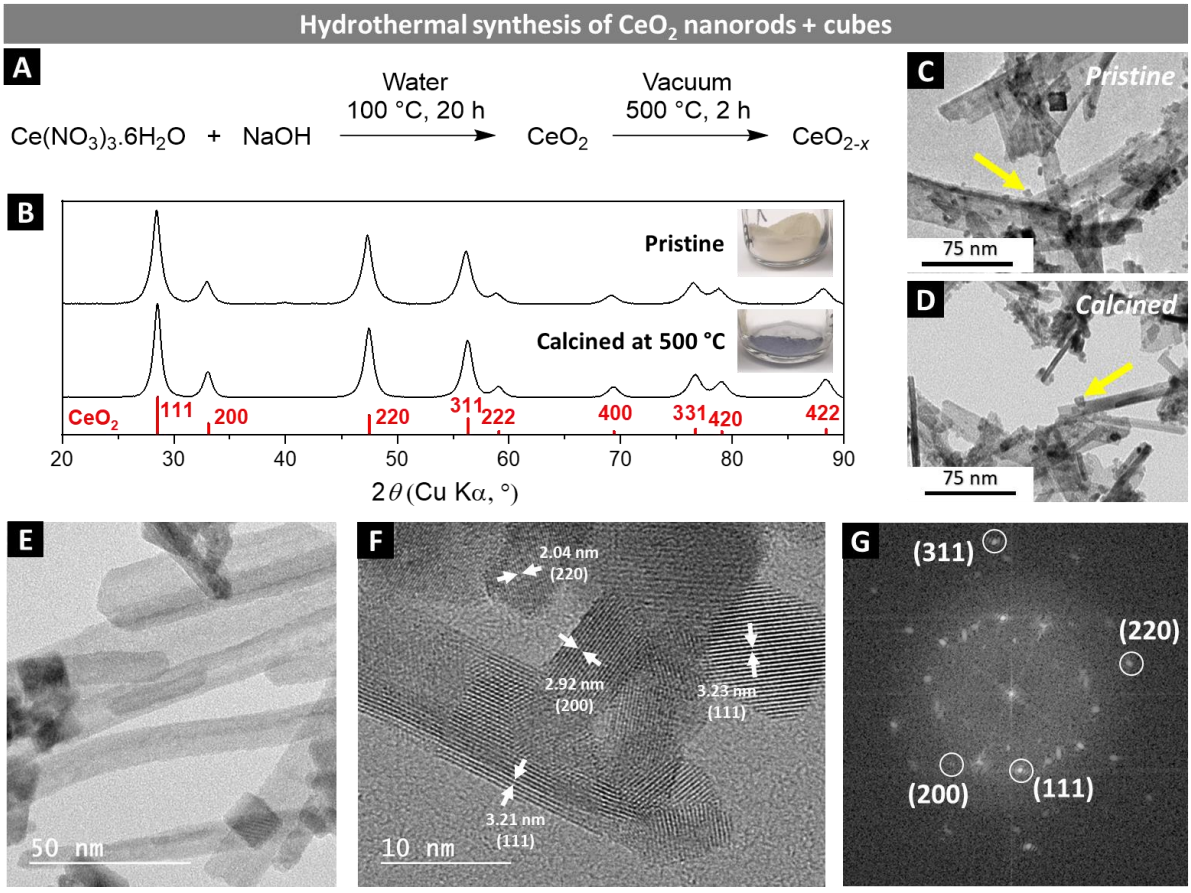

Figure 1. Synthesis of CeO_2 nanorods + cubes and subsequent calcination. (A) Reaction scheme. (B) XRD of the powders before (top) and after (bottom) calcination with lattice planes attribution, and pictures of the powders stored in argon. (C,D) TEM images of respectively the pristine sample and the

sample calcined at 500 °C (yellow arrows point at cubes). (E,F) HRTEM images of the pristine sample with attributed diffraction fringes, and (G) corresponding Fourier transform.

To compare ceria nanoparticles produced following different pathways, we expanded the study to a second material originating from the calcination of cerium oxyhydroxide $CeO(OH)_2$. This material was produced *via* a hydrothermal synthesis in absence of air (**Figure 2A,B**).[19] Such a CeO_{2-x} catalyst was recently reported by Qu *et al.* for its outstanding catalytic activity in liquid phase hydrogenation, likely due to the accommodation of a large concentration of defective Ce^{3+} sites.[6] The TEM analysis revealed nanorods of similar dimensions (100–200 nm long × 10–30 nm wide) but no cubes (**Figure 2C**). According to XRD, the $CeO(OH)_2$ NPs evolved into ceria after calcination at 200 °C, with slightly smaller crystallites than the first sample considering the broader diffraction peaks (**Figure 2B**). The global nanorods/nanoplates morphology was preserved, and numerous defects appeared as dark spots, as reported in the literature (**Figure 2D**).[6]

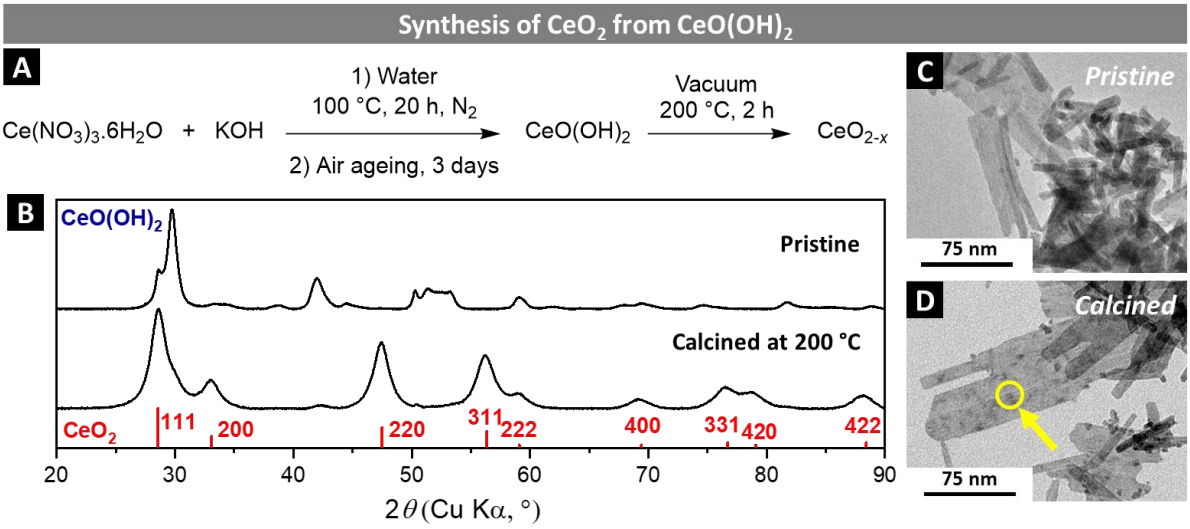

Figure 2. Synthesis of CeO_2 nanoparticles from $CeO(OH)_2$. (A) Reaction scheme. (B) XRD of the powders before (top) and after (bottom) calcination with lattice planes attribution. (C,D) TEM images of respectively the pristine sample and the sample calcined at 200 °C (yellow arrow points at a defect).

2.2. Cerium oxide reduction upon calcination

The evolution of the oxidation state of Ce and O at the surface of the ceria samples was monitored using the NAP-XPS of Sorbonne Université set on the beamline TEMPO-B of the SOLEIL synchrotron. The sample consisted of non-calcined nanoparticles drop-casted on a gold-coated silicon wafer from an ethanolic suspension (**Figure 3A**). The setup of the analysis chamber allowed the monitoring of the calcination step *in vacuo*, followed by exposure to H_2, without any sample transfer step (**Figure 3B**). A photon energy of E_{hv} = 1100 eV was chosen to study both the Ce 3d and O 1s regions, corresponding to electron kinetic energies of respectively *ca.* E_{kin} = 200 eV and E_{kin} = 570 eV (see **Figure S5** for a representative survey). These energies result in inelastic mean free paths (IMFP) of electrons in CeO_2 of *ca.* 0.7 nm and 1.3 nm, respectively, corresponding to probed depths of 2.1 nm and 3.9 nm (3 × IMFP).[24] As the probed volumes differed, no direct estimation of the Ce:O ratio was proposed.

Drop-casting of the powder resulted in the presence of aggregates, which made the data for the Ce 3d region noisier than what is typically obtained on single-crystals or well-prepared thin films (**Figure 3D**). However, the results directly reflect the surface reactivity of hydrothermally produced nanoparticles, more realistic for catalytic studies than CeO_2 films. As the usual Shirley algorithm led to irrelevant background estimation due to the ill-defined maxima positions, we adopted linear backgrounds defined on three regions. The Ce 3d spectra are typically composed of five doublets, two characteristic of Ce^{3+} and three of Ce^{4+} species (**Table S3** for fitting details).[2] Following the usual denomination, the two components of the spin-orbit coupling are noted V (Ce $3d_{5/2}$) and U (Ce $3d_{3/2}$), and the coupling values were estimated on the spectra: 18.35 eV for Ce^{3+} and 18.5 eV for Ce^{4+}, in agreement with the literature.[25] The peak positions were constrained on a range of approximately 0.5 eV around the expected position. The integration of the peak areas allows an estimation of the Ce^{3+}:Ce^{4+}

ratio, the error bar for this procedure being estimated at *ca.* 10 %. Note that the evolution of the Ce^{4+} fraction may be visually assessed for instance *via* the isolated contribution at 916 eV (orange) or the shape of the envelope.

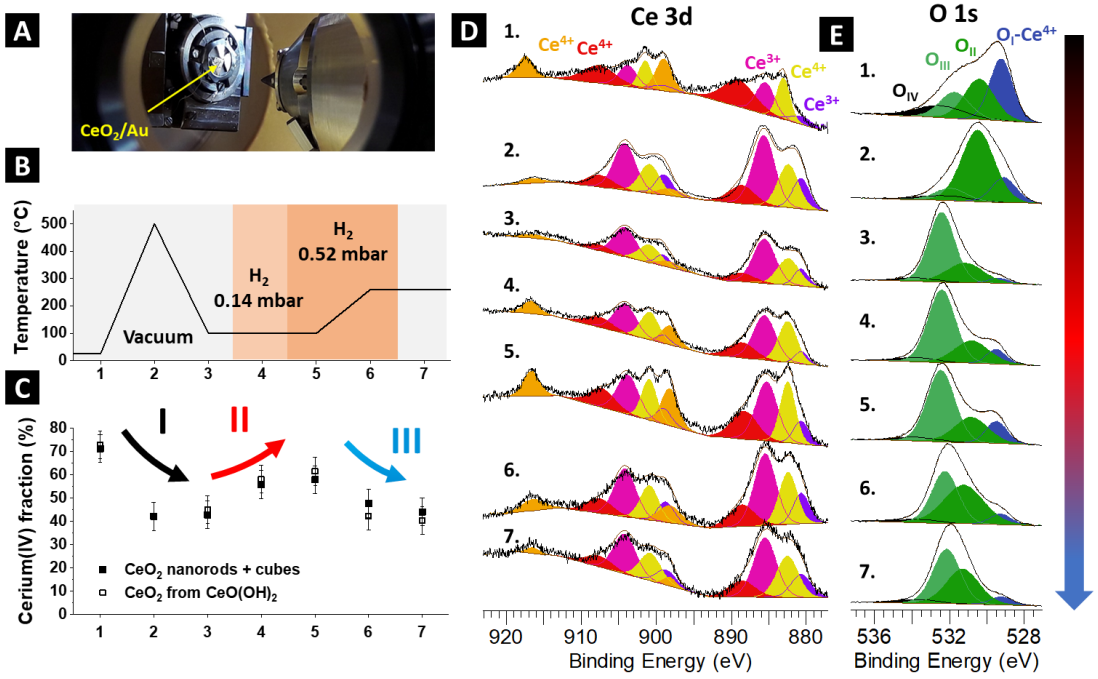

Figure 3. (A) Sample in the NAP-XPS analysis chamber used for *operando* data collection. (B) Graphic description of the treatment steps: (1) initial state at r.t., (2) 500 °C, (3) 100 °C, (4) 100 °C with H_2 0.14 mbar, (5) 100 °C with H_2 0.52 mbar, (6) 250 °C with H_2 0.52 mbar, (7) 250 °C in vacuum. (C) Evolution of the Ce^{4+} concentration at the material surface of the CeO_2 nanorods + cubes and of the sample deriving from $CeO(OH)_2$ calcination according to Ce 3d spectra deconvolution. (D) Ce 3d spectra recorded on the CeO_2 nanorods + cubes NPs. along the treatment. Color code: violet (V_0, U_0) and pink (V', U') for Ce^{3+}, yellow (V, U), red (V'', U''), and orange (V''', U''') for Ce^{4+}. (E) Corresponding O 1s spectra. Color code: blue (O_I adjacent to Ce^{4+}), green (O_{II} and O_{III} adjacent to Ce^{3+}), and black (O_{IV}, chemisorbed oxygen).

In the first step, the CeO_2 NPs (nanorods + cubes) were subjected to a thermal treatment up to 500 °C consisting of heating ramps of 10 °C/min and 1 h plateaus during which spectra were collected. The initial state (***1***) contains a Ce^{4+} fraction of 71 %, in line with a high density of defects and oxygen vacancies due to the limited size of the NPs (Figure 3**C**, black squares). A strong decrease in the Ce^{4+} fraction occurred upon temperature increase, down to 43 % at 500 °C (state ***2***). This evolution is coherent with the aforementioned color change from yellow to grey-violet for oven calcination of the material (Figure 1**B,** inset). The reduction essentially occurs below 400 °C and then stabilizes,

according to complementary spectra collected during the heating ramp (**Figure S6**. The oxidation state was not significantly modified upon cooling to 100 °C (final state ***3*** of the first part of the treatment), indicating the stability of the so-formed oxygen-defective cerium oxide. In UHV, the X-ray beam is known to induce a reduction of metals, such as cerium in CeO_2, to some extent. However, the most striking evolutions of the Ce 3d spectra occur after several hours exposed to UHV and dozens of minutes exposure to X-ray beam, suggesting the potential effect of beam damage remains limited in these changes and does not contradict the present analysis.[26] Overall, the described surface state evolutions in this article are consistent with previous works, including thin film analysis, which did not mention any beam damage effect.[17]

Such an increase in Ce^{3+} concentration upon calcination agrees with literature for a similar treatment (30 min at 500 °C under vacuum). For example, Freund *et al.* reported a progression of 6 % to 9.2 % of Ce^{3+} concentration for CeO_2 powder.[17] In the present case, the extent of the reduction was significantly higher as it reached 57 %. This difference is attributed to the smaller characteristic size of the particles and the higher density of defects and grain boundaries, compared with a commercial powder. Besides, according to DFT calculations, the formation energy of surface oxygen vacancies on CeO_2 follows the order: {110} (rods) > {100} (cubes) > {111} (polyhedra).[27]

The O 1s spectra were deconvoluted in four components: an O_I component (blue) at 529.2 eV, attributed to lattice oxygens linked to Ce^{4+} atoms, two components, O_{II} and O_{III} (green), at 530.1 eV and 531.4 eV, and a broad component O_{IV} (black) at 532.5 eV, merely not visible in these spectra and ascribed to chemisorbed oxygen (*e.g.* hydroxyl groups, water, carbonates) (Figure 3**E** and **Table S4** for fitting details)). The O_{IV} component was only observed in state ***1***, prior to any treatment. There is consensus in the literature on the attribution of O_I but not on those of O_{II} and O_{III}. While studying the reduction of CeO_2 films,

Reichling *et al.* thus deconvoluted the O 1s spectra with four peaks, as in the present work, and attributed the two ones of medium energies (O_{II} and O_{III}) to oxygens adjacent to Ce^{3+}.[28] In this context, the presence of Ce^{3+} was explained by surface defects consisting of oxygen vacancies. Considering the difficulty in accurately ascribing chemical species to all components and because of the contribution of oxygen from adventitious species, we limited our study to the qualitative analysis of the evolution of the O_I:(O_{II}+O_{III}) ratio. Upon calcination to 500 °C, this ratio decreased, accounting for the formation of defects and the reduction of Ce^{4+} in Ce^{3+}, in agreement with conclusions drawn from the Ce 3d spectra. The $CeO(OH)_2$ nanoparticles were deposited the same way and subjected to the thermal treatment during the same run, with very similar evolution of the Ce^{3+} concentration (Figure 3**C**, open squares).

2.3. Hydrogen activation on reduced CeO_2

In a second step, the so-formed reduced CeO_2 NPs were exposed to an H_2 pressure. As cerium oxide charged under the X–ray beam at low temperatures, we measured the initial state at 100 °C. Then, we added a moderate pressure of H_2 (0.14 mbar then 0.52 mbar), increased the temperature up to 250 °C, and finally removed H_2 (Figure 3**B-E**). We chose a final temperature of 250 °C to approach the operating conditions of acetylene semi-hydrogenation developed by Pérez-Jamírez *et al.*[29] Upon exposure to 0.14 mbar of H_2 at 100 °C, the deconvolution of Ce 3d XPS spectra indicates that the cerium atoms are oxidized to Ce^{4+} with a surface concentration increasing from 43 % (state ***3***) to 54 % (state ***4***). Increasing the H_2 pressure up to 0.52 mbar further increased the Ce^{4+} concentration to 58 % (state ***5***), revealing that the {CeO_2–H_2} system is still in the dynamic range at 0.12 mbar as to H_2 dissociation on the surface and has not reached saturation yet. However, heating to 250 °C (state ***6***) induced a reduction, with the concentration of Ce^{4+} down to 48 %, close to the level prior to exposure to H_2 (state ***3***). The removal of H_2 gas (state ***7***) slightly decreased the

proportion of oxidized cerium atoms down to 44 %. If the final Ce 3d spectrum at 250 °C is similar to the one before exposure to H_2, indicating some degree of reversibility of the hydride formation, the surface is still more oxidized than the one analyzed at 250 °C during the thermal treatment. The exposure to H_2 0.52 mbar is thus not sufficient to restore a surface state similar to the one obtained before calcination at 500 °C. Considering the visual evolution observed *ex situ* on the calcined sample exposed back to ambient conditions (Figure 1**B,** inset), we would nonetheless expect a partial reoxidation of the Ce^{3+} in Ce^{4+} upon air exposure.

In the O 1s spectra, the main feature is the growth of the O_I blue component from state ***3*** to state ***5***, *i.e.* upon increased H_2 pressures, followed by its decrease back to a similar level to state ***3*** upon heating to 250 °C. As this component is associated with oxygen in an oxidized environment, *i.e.* linked to Ce^{4+} atoms, this observation supports the Ce^{3+}:Ce^{4+} ratio analysis from Ce 3d spectra. Our observations thus agree with the mechanism of H_2 adsorption-induced oxidation of reduced CeO_2 reported by Freund *et al.*[17] As for the calcination step, the extent of the phenomenon is much higher in our case, with a Ce^{4+} concentration increasing by 15 % in the presence of 0.52 mbar of H_2 and then decreasing by 14 % upon temperature increase.

The analysis of the Ce 3d spectrum of the CeO_2 derived from $CeO(OH)_2$ displayed a similar evolution of the Ce^{4+} surface concentration and hydride formation, with an increase of 16 % in presence of H_2 followed by a decrease of 21 % upon temperature increase (Figure 3**D and Figure S7**). This confirms the robustness of the scale of the observed phenomenon. This also suggests the formation of a high number of hydrides when compared with literature results, comes from a shared origin: the high concentration of defects generated upon thermal treatment, promoted by the limited crystallinity and the large number of grain boundaries.

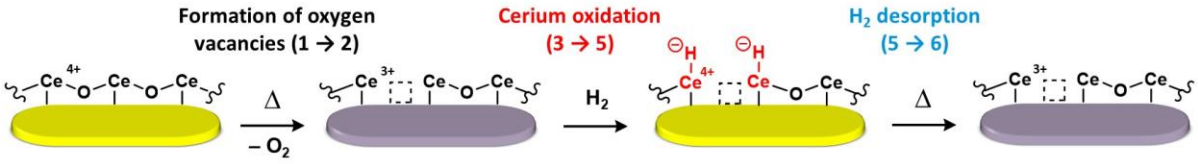

Scheme 1. Mechanistic proposal for the changes of cerium oxidation state (yellow: Ce^{4+}-rich, grey-purple: Ce^{3+}-rich). Numbers corresponds to steps presented in Figure 3.

In summary, the calcination of CeO_2 under vacuum led to the formation of surface Ce^{3+} atoms *via* the formation of O_2 and oxygen vacancies (Eq. (5)) (Scheme 1). These vacancies may then adsorb H_2 (Eq. (6)) and activate it to form cerium hydride species (Eq. (7)). Considering the increase in the oxidation state of the cerium, the hydrogen atoms are thought to be electron-rich, hence the hydride terminology.[17] Upon heating, typically above 250 °C, the hydride species recombine as H_2 and desorb from the cerium oxide (reverse Eq. (7) and (6)), or recombine with oxygen to form water (Eq. (8)), accompanied by the reduction of cerium sites.

$$2\,Ce^{4+} + O^{2-} \xrightarrow{>100\,°C} 2\,Ce^{3+} + V_O + \frac{1}{2}O_2 \quad (5)$$

$$V_O + H_2 \longrightarrow H_{2\,V_O}^{*} \quad (6)$$

$$Ce^{3+} + \frac{1}{2}\,H_{2\,V_O}^{*} \xrightarrow{<250\,°C} (Ce^{4+} - H_{V_O}^{-}) \quad (7)$$

$$2\,(Ce^{4+} - H_{V_O}^{-}) + O^{2-} + 2\,Ce^{4+} \longrightarrow 4\,Ce^{3+} + 3\,V_O + H_2O \quad (8)$$

By coupling XPS and electron spin resonance (ESR) experiments with DFT calculations, Freund *et al.* demonstrated that the stability of surface hydrides increases with the concentration of oxygen vacancies for CeO_2(111) (polyhedra morphology).[10] A similar result was reported by Lu *et al.* for CeO_2(110) facets (rods morphology): a high enough defect concentration shifted the main H_2 activation mechanism from a homolytic one, forming two hydroxyls groups, to a heterolytic one at solid FLP sites (thus implying a surface hydride).

Such hydride species allowed lower activation energies for hydrogenation reactions, for instance of acetylene,[12] and led to higher conversions. Unfortunately, the selectivity toward the desired ethylene was drastically decreased due to the formation of the over-hydrogenated ethane and to the coupling of carbon adsorbed species, making undesirable the formation of too many oxygen vacancies. Active sites for H^- species formation are still interesting as they are at the origin of the good selectivity of reduced ceria for crotonaldehyde hydrogenation to crotyl alcohol.[9] In addition, the stabilization of H^- on Ce^{3+} rich ceria is thoroughly investigated to generate efficient solid-state FLPs catalysts.[6] Following the first experimental promising results, Qu *et al.* explored the role of the exposed facet by DFT calculations and the rate-determining barrier of acetylene hydrogenation decreases from 0.88 eV for reduced CeO_2(100) to 0.58 eV for reduced CeO_2(110), suggesting a better performance for the nanorod morphology.[30] Overall, the choice of the facet mainly exposed and the beneficial *vs.* detrimental effect of large concentration of surface oxygen vacancy as to hydride stabilization appear to be highly dependent on the targeted mechanism (homolytic *vs.* heterolytic). By providing a methodology for direct assessment of this question, the present work should contribute to a clever use of CeO_2 nanoparticles as hydrogenation catalyst.

4. Conclusion

The present work first unambiguously confirmed by NAP-XPS the experimental observation of Freund *et al.* as to the oxidation of reduced ceria by incorporation of H_2 as surface hydrides. The results were here recorded on two defective CeO_2 nanorods synthesized following a hydrothermal pathway. The direct observation of the formation of surface hydride on realistic CeO_2 materials for catalysis was essential, in our opinion, considering the high expectations deriving from their potential for semi-hydrogenation catalysis. Besides, we showed that the extent of the H_2 activation may be drastically increased depending on the nature of the ceria nanoparticles, for instance, their morphology. Here, the significantly higher

Ce^{3+} surface concentration upon calcination, and subsequent oxidation in the presence of H_2, are expected to be due to a higher density of defects (polycrystalline NPs) and surface singularities. The exposed facets, directly depending on the morphology of the particles, may also play a critical role in the H_2 splitting activation energy. By supporting a recently unveiled mechanism, this *operando* NAP-XPS study will help the community to develop optimal syntheses for the preparation of CeO_2 catalysts for H_2 activation as surface hydride species, and their subsequent use for hydrogenation reactions.

5. Experimental section

Chemicals. All chemicals were used as received without further purification. $Ce(NO_3)_3 \cdot 6H_2O$ (99.5 %), NaOH (98 %), and KOH (85 %) were purchased from Alfa Aesar and the ethanol (96 %) from VWR. Distilled water was prepared using a Merck Milli-Q system (25 MΩ/cm).

CeO_2 NPs synthesis. In a 250 mL Borosilicate vessel, 3.91 g of $Ce(NO_3)_3 \cdot 6H_2O$ (9 mmol, 1 equiv.) were dissolved in 30 mL of distilled water to yield a colorless limpid solution. Meanwhile, 43 g of NaOH pellets (1.075 mol, 6 M) were dissolved in 150 mL of water and the resulting solution was slowly added to the cerium nitrate solution. A yellow-brown precipitate appeared at the first drops, followed by a yellow gel a grey gel, and finally a violet suspension. The turbid violet solution was stirred for 30 min and distributed in 4 Nalgene vessels of 50 mL not perfectly sealed to avoid autogenous pressure, which was then put in a preheated oven at 100 °C for 20 h. After the reaction, the solution was let to cool down naturally to r.t. A grey-violet powder sedimented at the bottom of the vessel, the supernatant was colorless. The whole suspensions were brought together and centrifugated (9,000 rpm, 10 min, 20 °C). The grey powder was washed 6 times with 30 mL of H_2O and

once with 30 mL of EtOH: along the washings, the powder gradually turned beige. The obtained beige powder (1.45 g, 94 % yield) was then dried under N_2 and stored under air. The synthesis of $CeO(OH)_2$ is similar by substituting the NaOH base by KOH and by performing the reaction in absence of air, as reported in a previous work.[19]

Thermal treatments. The synthesized CeO_2 material was placed in a Schlenk tube whose atmosphere was evacuated down to a primary vacuum. The tube was then placed in a preheated oil bath (100 °C or 200 °C) for 2 h and reopened after cooling down only in an Ar-filled glovebox. A similar procedure was followed for the treatment at 500 °C with a metallic heating mantle.

Materials characterization. Powder X–Ray Diffraction (XRD) measurements were performed on a Bruker D8 Advance diffractometer, using Cu Kα radiation at 1.5406 Å, with steps of 0.05° and a scanning rate of 1°/min. Physisorption measurements were performed on a Quantachrome Quadrasorb SI apparatus with N_2 adsorption at 77 K after degassing at 150 °C during 15 h. The specific surface area (S_{BET}) was obtained from the N_2 adsorption data ($P/P_0 < 0.2$) using the Brunauer–Emmett–Teller (BET) method. For Transmission Electron Microscopy (TEM) analysis, a drop of a diluted solution of nanoparticles dispersed in ethanol was allowed to dry on an amorphous carbon-coated copper grid. TEM images were acquired with a TWIN 120 (TECNAI SPIRIT) operating at 120 kV. HRTEM images were acquired with a JEOL 2100Plus, operating at 200 kV and equipped with a LaB_6 gun. Laboratory XPS spectra were collected on an Omicron Argus X-ray photoelectron spectrometer, using a monochromated Al K_α ($h\upsilon$= 1486.6 eV) radiation source having a 300 W electron beam power. The samples were analyzed under ultra-high-vacuum conditions (10^{-8} Pa). After recording a broad range spectrum (pass energy, 100 eV), high-resolution spectra were recorded for the Ce 3d, C 1s, and O 1s core XPS levels (pass energy, 20 eV). The binding energies were calibrated with respect to the C 1s peak at 284.5 eV. NAP-XPS was performed

on the TEMPO B beamline at SOLEIL on the setup of Sorbonne Université. The samples were deposited by drop casting from an ethanolic suspension of nanoparticles well dispersed by sonication onto a gold-coated silicon wafer, as commonly done for deposited nanoparticles analysis.[31] The presence of the gold layer favors the drainage of photo-generated charges from the nanoparticles, without reported influence on the surface reactivity of the drop-casted material. The variation of the background through measurements may be related to a remaining limited charging effect on few aggregates at low temperature but does not prevent deconvolution. Spectra were measured under vacuum (10^{-9} mbar), under 0.14 mbar or 0.52 mbar of H_2 with a photon energy of 1100 eV. Hydrogen (purity > 99.99 %) was introduced through a leak valve. After recording a broad range spectrum (pass energy, 50 eV), high-resolution spectra were recorded for the C 1s, O 1s, Au 4f, and Ce 3d core XPS levels (pass energy, 20 eV). The binding energies were calibrated with respect to the Au 4f doublet peak at 84.0 eV, which appeared symmetrical, pointing at the absence of strong charging effect. Spectrum processing was carried out using the CasaXPS software package.

6. List of contributions

R. F. A. conducted the syntheses and the XPS data treatment. The NAP-XPS setup was managed by J.-J. G. and F. B., and operated by all authors for the data collection. R. F. A. and S. C. conceived the project and co-wrote the manuscript, S. C. spearheading it. All authors approved the final version of the manuscript.

7. Conflict of interest

The authors declare no conflict of interest.

8. Acknowledgements

This project has received funding from the European Research Council (ERC) under the European Union's Horizon 2020 research and innovation program (Grant agreement No. 758480). This work was supported by Sorbonne Université and CNRS. We acknowledge the

TEMPO beamline at Synchrotron SOLEIL for beamtime (proposal 20200266). We acknowledge Antoine Pesesse, Anthony Ropp, Alberto Palazzolo and Alexy Freitas for their contribution to NAP–XPS data acquisition. We acknowledge Ferdaous Ben Romdhane for the HRTEM data acquisition, and Antoine Miche for the laboratory XPS data acquisition.

9. References

[1] D. R. Mullins, *Surf. Sci. Rep.* **2015**, *70*, 42–85.
[2] X. Garcia, L. Soler, N. J. Divins, X. Vendrell, I. Serrano, I. Lucentini, J. Prat, E. Solano, M. Tallarida, C. Escudero, J. Llorca, *Catalysts* **2020**, *10*, 286.
[3] K. Reed, A. Cormack, A. Kulkarni, M. Mayton, D. Sayle, F. Klaessig, B. Stadler, *Environ. Sci. Nano* **2014**, *1*, 390–405.
[4] J. Kammert, J. Moon, Z. Wu, *Chinese J. Catal.* **2020**, *41*, 901–914.
[5] G. Vilé, S. Wrabetz, L. Floryan, M. E. Schuster, F. Girgsdies, D. Teschner, J. Pérez-Ramírez, *ChemCatChem* **2014**, *6*, 1928–1934.
[6] S. Zhang, Z. Huang, Y. Ma, W. Gao, J. Li, F. Cao, L. Li, C. Chang, Y. Qu, *Nat. Commun.* **2017**, *8*, 1–11.
[7] G. Vilé, B. Bridier, J. Wichert, J. Pérez-Ramírez, *Angew. Chemie Int. Ed.* **2012**, *51*, 8620–8623.
[8] G. Vilé, S. Colussi, F. Krumeich, A. Trovarelli, J. Pérez-Ramírez, *Angew. Chemie Int. Ed.* **2014**, *53*, 12069–12072.
[9] Z. Zhang, Z.-Q. Wang, Z. Li, W.-B. Zheng, L. Fan, J. Zhang, Y.-M. Hu, M.-F. Luo, X.-P. Wu, X.-Q. Gong, W. Huang, J.-Q. Lu, *ACS Catal.* **2020**, *10*, 14560–14566.
[10] Z. Li, K. Werner, L. Chen, A. Jia, K. Qian, J. Zhong, R. You, L. Wu, L. Zhang, H. Pan, X. Wu, X. Gong, S. Shaikhutdinov, W. Huang, H. Freund, *Chem. – A Eur. J.* **2021**, *27*, 5268–5276.
[11] Z. Wu, Y. Cheng, F. Tao, L. Daemen, G. S. Foo, L. Nguyen, X. Zhang, A. Beste, A. J. Ramirez-Cuesta, *J. Am. Chem. Soc.* **2017**, *139*, 9721–9727.
[12] Z. Li, L. Chen, Z. Wu, A. Jia, S. Shi, H. Zhang, J. Wang, Z. Liu, W.-P. Shao, F. Yang, X.-P. Wu, X.-Q. Gong, W. Huang, *ACS Catal.* **2023**, *13*, 5213–5224.
[13] Z. Zhou, L. Chen, L. Wang, Y. Liu, P. Cheng, H. Peng, J. Cai, Q. Zhou, Y. Wang, N. Yang, B. Wang, X.-Q. Gong, F. Yang, Z. Liu, *ACS Catal.* **2023**, *13*, 9588–9596.
[14] Z.-Q. Wang, D.-R. Chu, H. Zhou, X.-P. Wu, X.-Q. Gong, *ACS Catal.* **2022**, *12*, 624–632.
[15] A. Ben Yaacov, L. J. Falling, R. Ben David, S. Attia, M. A. Andrés, S. Nemšák, B. Eren, *J. Phys. Chem. Lett.* **2023**, *14*, 7354–7360.
[16] B. Wang, L. Zhang, J. Cai, Z. Peng, P. Cheng, X. Li, H. Zhang, F. Yang, Z. Liu, *Adv. Mater. Interfaces* **2021**, *8*, 2002169.
[17] Z. Li, K. Werner, K. Qian, R. You, A. Płucienik, A. Jia, L. Wu, L. Zhang, H. Pan, H. Kuhlenbeck, S. Shaikhutdinov, W. Huang, H. Freund, *Angew. Chemie Int. Ed.* **2019**, *58*, 14686–14693.
[18] K. Werner, X. Weng, F. Calaza, M. Sterrer, T. Kropp, J. Paier, J. Sauer, M. Wilde, K. Fukutani, S. Shaikhutdinov, H.-J. Freund, *J. Am. Chem. Soc.* **2017**, *139*, 17608–17616.
[19] R. F. André, G. Rousse, C. Sassoye, M. Avdeev, B. Lassalle-Kaiser, B. Baptiste, S. Carenco, *Chem. Mater.* **2023**, *35*, 5040–5048.
[20] H.-X. Mai, L.-D. Sun, Y.-W. Zhang, R. Si, W. Feng, H.-P. Zhang, H.-C. Liu, C.-H. Yan, *J. Phys. Chem. B* **2005**, *109*, 24380–24385.

[21] Y. Xu, S. S. Mofarah, R. Mehmood, C. Cazorla, P. Koshy, C. C. Sorrell, *Mater. Horizons* **2021**, *8*, 102–123.
[22] C. Yang, X. Yu, S. Heißler, A. Nefedov, S. Colussi, J. Llorca, A. Trovarelli, Y. Wang, C. Wöll, *Angew. Chemie Int. Ed.* **2017**, *56*, 375–379.
[23] R. Wang, R. Dangerfield, *RSC Adv.* **2014**, *4*, 3615–3620.
[24] M. Krawczyk, M. Holdynski, W. Lisowski, J. W. Sobczak, A. Jablonski, *Appl. Surf. Sci.* **2015**, *341*, 196–202.
[25] E. Bêche, P. Charvin, D. Perarnau, S. Abanades, G. Flamant, *Surf. Interface Anal.* **2008**, *40*, 264–267.
[26] M. A. Isaacs, C. Drivas, R. Lee, R. Palgrave, C. M. A. Parlett, D. J. Morgan, *Appl. Surf. Sci. Adv.* **2023**, *18*, 100469.
[27] T. Cao, R. You, Z. Li, X. Zhang, D. Li, S. Chen, Z. Zhang, W. Huang, *Appl. Surf. Sci.* **2020**, *501*, 144120.
[28] C. Barth, C. Laffon, R. Olbrich, A. Ranguis, P. Parent, M. Reichling, *Sci. Rep.* **2016**, *6*, 21165.
[29] D. Albani, M. Capdevila-Cortada, G. Vilé, S. Mitchell, O. Martin, N. López, J. Pérez-Ramírez, *Angew. Chemie Int. Ed.* **2017**, *56*, 10755–10760.
[30] Z. Huang, L. Liu, S. Qi, S. Zhang, Y. Qu, C. Chang, *ACS Catal.* **2018**, *8*, 546–554.
[31] S. Carenco, C. Sassoye, M. Faustini, P. Eloy, D. P. Debecker, H. Bluhm, M. Salmeron, *J. Phys. Chem. C* **2016**, *120*, 15354–15361.

Table of Content Graphic